Alternative Nonlocal Descriptions of Boundary-Layer Evolution

QING ZHANG AND ROLAND STULL

Boundary Layer Research Team, Department of Atmospheric and Oceanic Sciences, University of Wisconsin—Madison, Madison, Wisconsin

(Manuscript received 24 May 1991, in final form 24 January 1991)

ABSTRACT

Two alternative parameterizations for nonlocal turbulence mixing are tested in a 1D boundary-layer model against a dataset from the 1983 Boundary-Layer Experiment (BLX83) in Oklahoma. One method, proposed previously by Stull and Driedonks, is based on a nonlocal approximation to the turbulence kinetic energy (TKE) equation. An alternate method, based on a nonlocal approximation to the Richardson number, is simplified here from earlier parameterizations for transilient turbulence theory. Convective mixed-layer simulations of the vertical profiles of mean variables and fluxes using both methods are compared to the BLX83 observations and to simulations using a traditional slab model.

The TKE method develops a surface layer that is too thick compared to BLX83 data, particularly in the early morning. It also lacks the subadiabatic lapse rate that is observed in the top of the mixed layer. The Richardson number approach produces more accurate mixed-layer profiles, but lacks the general physical interpretation of the TKE method. Nonlocal spectral decompositions of the flux and intensity of mixing confirm that large-size eddies dominate within the middle of the mixed layer. Based on this limited validation, the Richardson number method is recommended for convective boundary layers, but the TKE approach should be used for modeling more general boundary layers that can include clouds and stable and/or windy conditions.

1. Introduction

Boundary-layer models all require some form of turbulence closure approximation. Local first-order closure theories have been well tested and their capabilities and limitations quantified since their introduction in the 1930s. Nonlocal first-order approaches such as transilient turbulence theory (Stull 1984) are more recent and have yet to be tested over similarly wide ranges of applications and conditions. Also, only a couple nonlocal parameterizations have been presented in the literature.

In this paper, data from a unique field experiment, the 1983 Boundary-Layer Experiment (BLX83), are used to measure the capabilities of two alternative transilient turbulence parameterizations within the framework of a one-dimensional boundary-layer model. BLX83 is unique because it attempted to measure mean subsidence along with the usual remote and in situ measurements of fluxes and mean profiles. In addition, it utilized line-averaged lidar scans and slant ascent/descent aircraft soundings to overcome the large sampling inaccuracies of mixed-layer (ML) depth z_i associated with point rawinsonde observations.

We are looking beyond whether the transilient models give boundary-layer evolution that looks generally reasonable to ask which parameterization most accurately describes the precise conditions observed during a BLX83 case-study day. For the previously published turbulence kinetic energy (TKE) parameterization, this is performed without tuning any model parameters. A new formulation of a nonlocal Richardson number parameterization is also tested. Simulations using both nonlocal parameterizations are also compared to those from a zero-order closure mixed-layer (slab) model.

Such information on model accuracy and limitations is useful so that the model can be used confidently in more complex climate simulations and dispersion calculations.

2. BLX83 experiment

BLX83 ran from 25 May 1983 through 18 June 1983 in Oklahoma, and was designed to study the turbulence structure in the boundary layer and its interaction with fair-weather cumulus clouds. A variety of data was collected using an instrumented aircraft, portable automated mesonet stations (PAM II), radiosondes, a flux tower, and a lidar (Stull and Eloranta 1984). Most of the sensors were located near a central field site 8 km east of the town of Chickasha at 35.03°N, 97.86°W, and elevation 325.8 m (MSL). This site marks the location of the model simulations.

Radiosondes were launched during the daytime from Canton, Ft. Sill, Shawnee, and Oklahoma City to get soundings of wind, temperature, and humidity. Canton

Corresponding author address: Roland Stull, Boundary Layer Research Team, Dept. of Atmospheric and Oceanic Sciences, University of Wisconsin, 1225 W. Dayton St., Madison, WI 53706.

is 130 km NW of the field site, Ft. Sill is 75 km SW of the site, and Shawnee is 80 km east-northeast. These three research launch sites formed a triangle around the center site. At Oklahoma City, in the triangle interior, the National Weather Service launched their routine 0000 and 1200 UTC rawinsondes.

The NCAR Queen Air instrumented aircraft made a series of horizontal flight legs at different levels ranging from 50 m above ground level (AGL) to the top of the ML, and made ascending and descending slant soundings. The 50-m elevation flight legs are particularly useful for estimating surface fluxes. Thirteen PAM II stations around the Chickasha area collected near-surface temperature, humidity, pressure, wind, and rainfall data at 5-minute intervals. An instrumented tower operated by Argonne National Laboratory (ANL) obtained the half-hour-averaged heat, moisture, and momentum fluxes at a height of 5.17 m using eddy-correlation techniques. The University of Wisconsin—Madison (UW) lidar was located near the Chickasha central site to observe rising thermals, mixed-layer thickness, and other turbulence structures by using the spatial distributions of aerosol concentrations as tracers of vertical air motion. The National Severe Storms Laboratory Doppler radar in Norman, Oklahoma, collected divergence data.

A cloudless day with sufficient measurements, 28 May 1983, was chosen as the case-study day. On this day most of the sensors were operational, and good data were collected. This day has already been extensively analyzed in support of other research goals. The reader is referred to Hechtel et al. (1990), Wilde et al. (1985), Crum et al. (1987), and Nelson et al. (1989) for more details.

The synoptic weather analysis at 1000 CDT (central daylight time = UTC − 5 h) for this day showed that Oklahoma was located in the warm sector of a developing storm system located about 700 km to the northeast of Chicksha. A dryline passed the BLX site the night before, bringing in drier air over the central plains. At 1900 CDT, a cold front approached to within 130 km north of the BLX region. Winds were light and the sky was clear at that time. Weather conditions during this quiet period provided the initial and boundary conditions for the various model tests.

3. Meteorological conditions

a. Initial conditions

Seven radiosondes were launched from 0600 to 1900 CDT at three stations on the case study day. The early morning soundings of potential temperature θ, specific humidity q, and eastward and northward wind components U and V at Canton at 0600 CDT and at Oklahoma City at 0700 CDT were averaged at the same heights to supply the initial conditions for the models (Fig. 1), and later soundings allowed comparison with the modeled profiles.

b. Boundary conditions

Heat, moisture, and momentum fluxes at the surface are prescribed as model boundary conditions based on surface observations from the BLX83 field experiment. Subsidence is prescribed at the top of the model according to observed divergence. Interior forcings that vary with height include the geostrophic wind and horizontal temperature gradient. These boundary conditions and forcings vary with time, and were determined as follows.

Surface sensible and latent heat fluxes during the day are obtained by combining the measurements of the Queen Air aircraft and ANL flux tower. An instrumented NCAR Queen Air aircraft (N306D) flew five

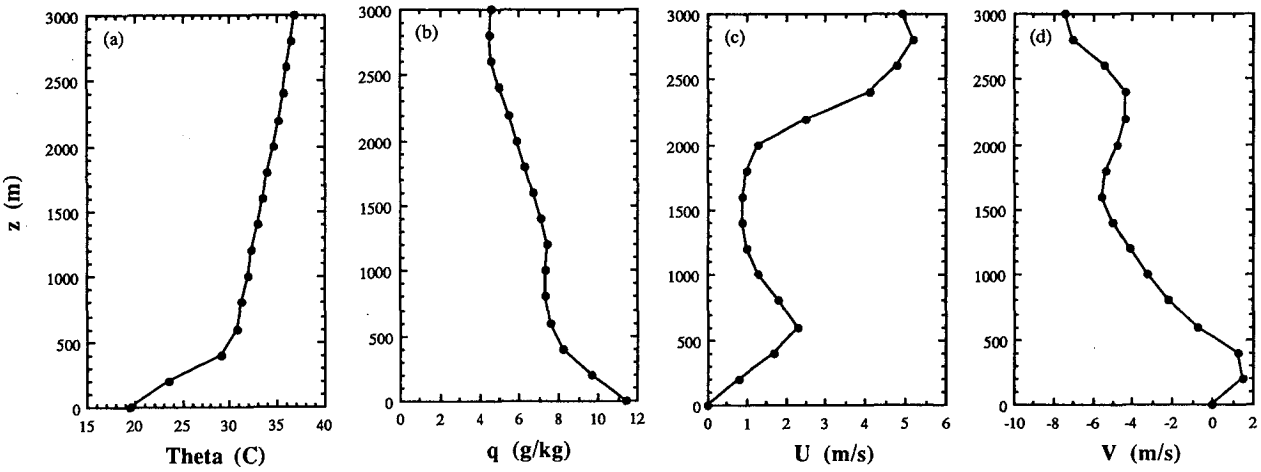

FIG. 1. Averaged observed vertical profiles of mean potential temperature (theta), specific humidity (q), and wind components (U, V) at 0600 CDT 28 May 1983 as model initial conditions.

near-surface flight legs during its 6-h "entrainment-zone" measurement mission. Temperature (T), specific humidity (q), and vertical velocity (w) were recorded 20 times per second using fast-response temperature, humidity, and wind sensors (Crum 1985). From these data, average values over each flight leg were found. After the linear trend and wavelengths longer than 6.5 km were filtered out, the turbulence departures T', w', and q' were calculated by subtracting the leg-mean values from the observed values. Then, turbulent kinematic fluxes $\overline{w'T'}$ and $\overline{w'q'}$ were found using eddy-correlation methods for each flight leg. One data point of $\overline{w'T'}$ and $\overline{w'q'}$ was obtained from each of the five near-surface flight legs flown at different times during the day.

Measured sensible heat flux Q_s^m, measured latent heat flux Q_l^m, and measured net radiation R_n^m were also observed by an instrumented tower operated by ANL. Eddy-correlation flux measurements of temperature, humidity, and momentum were taken at a height of 5.17 m after a 200-s running mean was removed from the data (Crum 1985). Half-hour–averaged Q_s^m, Q_l^m, and R_n^m were obtained from these eddy correlation fluxes between 0945 and 1915 CDT during the case study day.

Unfortunately, the ANL dataset was biased by systematic errors. Although the ANL data provided a long time series of high-resolution data that clearly showed the diurnal variation of fluxes, the data were later found by ANL to underestimate the magnitudes of the fluxes. The aircraft data was believed to be more accurate and representative of a larger area, but provided poor time resolution.

To utilize the best features of both datasets, the ANL data are used to determine only the diurnal time-evolution pattern of Q_s^m, Q_l^m, and R_n^m curves. The aircraft data are used to determine the relative magnitudes of the Q_s^m, Q_l^m, and R_n^m curves. The combined data were fit with a second-order polynomial during the daytime (appendix A). Then, the surface energy budget equation was used to modify these measured sensible heat and latent heat flux values to yield an energetically consistent balance:

$$R_n^m = Q_s + Q_l + Q_G \tag{1}$$

where R_n^m is net incoming radiation, Q_s is the adjusted upward sensible heat flux estimate, Q_l is the adjusted upward latent heat flux estimate, and Q_G is the flux down into ground. Assuming $Q_G = 0.1 R_n$ during daytime (Stull 1988) yields:

$$0.9 R_n^m = Q_s + Q_l. \tag{2}$$

Furthermore, the Bowen ratio for the adjusted values are assumed to equal the unadjusted ratio:

$$\frac{Q_s^m}{Q_l^m} = \frac{Q_s}{Q_l}. \tag{3}$$

Thus, (2) and (3) can be solved for Q_s and Q_l based on measured Q_s^m, Q_l^m, and R_n^m values to yield the final surface boundary conditions (Fig. 2). In summary, the ANL data determined the period of the diurnal curves, the aircraft data provided the ratio of Q_s to Q_l, and the energy budget was used to set the final amplitudes of Q_s and Q_l.

Surface geostrophic wind (U_g, V_g) and thermal wind (U_T, V_T) are calculated using multiple regression from horizontal pressure and temperature gradients based on the PAM II station data (Ferrare 1984). First, pressure and temperature measurements from the 13 PAM stations are adjusted to the altitude of the reference station, PAM station 1 at the central site. Next, plane surfaces are fit to the reduced pressure and temperature fields using least-squares to find the 2D linear horizontal gradients. The slope of the planes give $\partial P/\partial x$, $\partial P/\partial y$, $\partial T/\partial x$, and $\partial T/\partial y$. Then, half-hour–averaged U_g and V_g are calculated from these data (Fig. 3) (Hechtel 1988).

Instead of calculating geostrophic wind aloft from thermal wind as was done by Stull and Driedonks (1987), the revised model estimates the geostrophic wind profiles from the wind radio soundings by assuming the geostrophic wind aloft is equal to the actual wind above the ML. The wind observations at 1000 m and 2000 m are used because z_i is about 800 m in this case. The geostrophic wind profile at each time step is obtained by linear interpolation with height from the surface and two levels aloft, then with time from the six soundings.

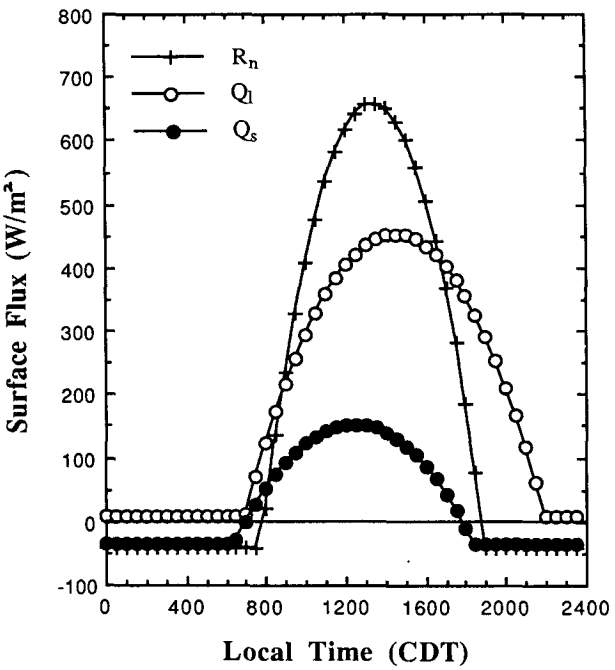

FIG. 2. Adjusted surface net radiation R_n, sensible heat flux Q_s, and latent heat flux Q_l applied as model boundary conditions for 28 May 1983.

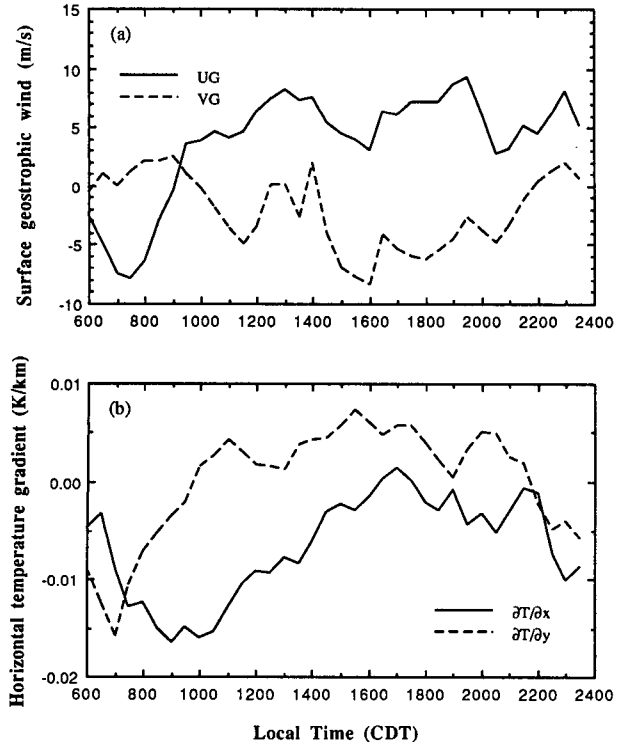

FIG. 3. Calculated surface boundary conditions: (a) geostrophic winds and (b) horizontal temperature gradients from observations at PAM II stations on 28 May 1983.

Surface momentum fluxes $\overline{u'w'}$ and $\overline{v'w'}$ are calculated using a drag coefficient approach:

$$\overline{(u'w')_s} = -C_D MU$$
$$\overline{(v'w')_s} = -C_D MV \qquad (4)$$

where $M = (U^2 + V^2)^{1/2}$; U and V are modeled wind speeds at lowest grid points; and drag coefficient C_D is based on static stability and surface roughness (Louis 1979). The average aerodynamic roughness length at the Chickasha central site is 0.20 m based on photographs of the land use at the PAM 1 site and utilizing the roughness chart, Fig. 9.6 of Stull (1988).

Subsidence $\bar{w}$ at the top of model is prescribed as a function of time, based on the divergence observations of Vachalek (1987), and is assumed to change linearly to zero at the ground. There is significant scatter in the subsidence data, but most sensors point to the same general trends, which are approximated by the line segments drawn in Fig. 4.

4. Model descriptions

The grid increments and domain for all three 1D models are identical. The center field site at Chickasha, Oklahoma, is chosen as the center of the model. Vertical grid increment size is $\Delta z = 100$ m, the vertical domain is 2000 m, and the time step is $\Delta t = 10$ min. The models are run from 0600 to 2000 CDT for the 28 May 1983 case.

a. Transilient model–TKE version

This model is identical to the transilient parameterization of Stull and Driedonks (1987) except the treatment of the geostrophic wind profile. To summarize, each time step is split into two parts. First, the external forcings such as dynamics, thermodynamics, and source and sink effects are applied as body forces and boundary conditions to destabilize the flow. For example, surface heat flux is applied at the bottom grid point as a boundary condition. Second, transilient theory responds to, and partly undoes, the instability. The amount of transilient turbulence is based on the instability quantified by a nonlocal approximation to the turbulence kinetic energy equation (TKE), and the resulting mixing is applied to all variables in the grid column. The model output contains profiles of mean variable and flux, such as θ, q, U, and V, and $\overline{w'T'}$, $\overline{w'q'}$, $\overline{u'w'}$, and $\overline{v'w'}$. The transilient coefficients c_{ij} are also saved at periodic intervals (Stull 1987).

The model equations and parameter values are the same as Stull and Driedonks's (1987). To summarize here, transilient coefficients c_{ij} are defined as:

$$c_{ij} = Y_{ij}/\|Y\| \quad \text{for} \quad i \neq j$$
$$c_{ii} = 1 - \sum_{\substack{j=1 \\ i \neq j}}^{n} c_{ij} \qquad (5)$$

where Y_{ij} is a symmetric matrix describing "mixing

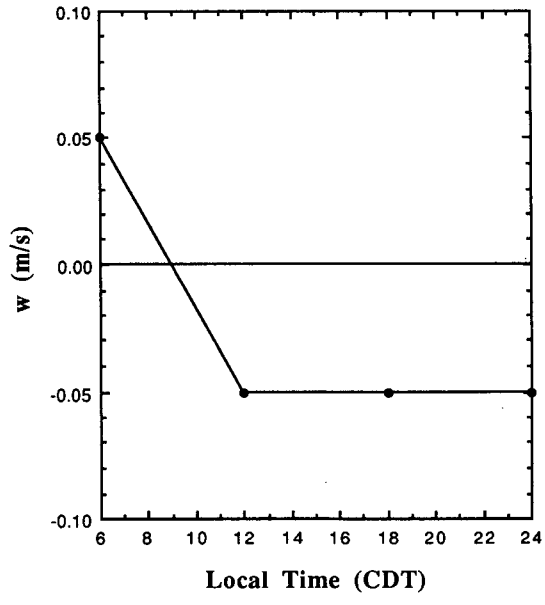

FIG. 4. Observed subsidence (positive upward) from divergence data on 28 May 1983 at the top of the model ($z = 2000$ m) applied as a boundary condition (Vachalek 1987).

potential" between any two boxes i and j, and $\|Y\|$ is a scalar norm (see Stull and Driedonks 1987). Matrix Y_{ij} is calculated from a nonlocal discrete approximation of the TKE equation:

$$Y_{ij} = \frac{\tau_0 \Delta t}{(z_i - z_j)^2}\left[(U_i - U_j)^2 + (V_i - V_j)^2 - \frac{g}{(\theta_{vi} - \theta_{vj})}\frac{(z_i - z_j)(\theta_{vi} - \theta_{vj})}{R_c}\right] - D\Delta t/\tau_0 \quad \text{for} \quad i \neq j \quad (6)$$

where τ_0 is a time scale of turbulence, R_c is a dimensionless parameter analogous to a critical Richardson number, and D is a dimensionless dissipation factor.

The internal mixing potential Y_{ii} is defined as

$$Y_{ii} = \max(Y_{i,i-1}, Y_{i,i+1}) + Y_{\text{ref}} \quad (7)$$

where the reference potential Y_{ref} is another parameter accounting for the potential for subgrid-scale internal mixing within box i.

Based on the calibration simulation in Cabauw case studies (Stull and Driedonks 1987), the four parameters were chosen as $\tau_0 = 1000$ s, $R_c = 0.21$, $D = 1$, and $Y_{\text{ref}} = 1000$. They remain the same value for the Oklahoma case in this model, since these four parameters are considered as universal constants.

b. *Transilient model—R_i version*

Stull (1984) originally proposed a nonlocal Richardson number R_i parameterization for the transilient coefficients, but it was embedded within a complicated set of matrix equations. A simpler Ri parameterization is presented here.

Use a nonlocal bulk Richardson number r_{ij} as a measure of the static and dynamic instability between the destination box i and the source box j:

$$r_{ij} = \left(\frac{g}{\theta_{ij}}\right)\frac{(\theta_i - \theta_j)(z_i - z_j)}{(U_i - U_j)^2 + (V_i - V_j)^2} \quad (8)$$

where $\theta_{ij} = (\theta_i + \theta_j)/2$. Furthermore, r_{ij} is assumed to be a symmetric matrix:

$$r_{ij} = r_{ji}. \quad (9)$$

A forcing matrix Y_{ij}, analogous to the "mixing potential matrix" Y_{ij} of Stull and Driedonks (1987), is constructed based on the nonlocal Richardson number r_{ij}:

$$Y_{ij} = w_{ij}\left[1 - \frac{r_{ij}}{R_T}\right] \quad (10)$$

where R_T is the turbulence termination Richardson number, and w_{ij} is defined as a distance weighting function:

$$w_{ij} = \frac{U_0 \Delta t}{|j - i|\Delta z} \quad \text{for} \quad i \neq j \quad (11)$$

that partially removes grid spacing and time-increment dependence from the model physics; U_0 is a characteristic scaling velocity assumed to be the same order of magnitude as the convective velocity scale w_*. The value of w_{ij} is truncated to fall between 0 and 1.

The mixing potential Y_{ij} is also truncated to the range of 0 (preventing unmixing when $r_{ij} > R_i$) and 1 (preventing convective overturning).

The transilient coefficient c_{ij} is then defined as:

$$c_{ij} = \frac{1}{n_d} Y_{ij} \quad \text{for} \quad i \neq j \quad (12a)$$

$$c_{ii} = 1 - \sum_{\substack{j=1 \\ j \neq i}}^{N} c_{ij} \quad (12b)$$

where N denotes the total number of grid points and n_d is the number of grid points within the subdomain that is turbulent at each time step. Both Y_{ij} and c_{ij} are symmetric matrices.

The values of the velocity scale $U_0 = 0.5$ m s^{-1}, the critical Richardson number for turbulence onset $R_i = 1.5$, and the termination Richardson number $R_T = 2.0$ are found to yield the most realistic forecasts in this case study. Justification for these values of critical Richardson numbers was given by Stull (1984), based on the finite grid-increment size. These values also gave good forecasts for the Cabauw data of Stull and Driedonks (not presented here). The rest of the model and the initial and boundary conditions remain the same as in section 4a.

c. *Slab model*

A simple mixed-layer slab model is tested in this paper using the same initial and boundary conditions as the transilient simulation model. The set of forecast equations are

$$z_i \frac{d\bar{\theta}}{dt} = \overline{w'\theta'_s} - \overline{w'\theta'_{z_i}} \quad (13a)$$

$$z_i \frac{d\bar{q}}{dt} = \overline{w'q'_s} - \overline{w'q'_{z_i}} \quad (13b)$$

$$\frac{dz_i}{dt} = w_e + w_l \quad (13c)$$

$$w_e = \frac{\overline{w'\theta'_{z_i}}}{\Delta\bar{\theta}} \quad (13d)$$

$$\overline{w'q'_{z_i}} = -w_e \Delta\bar{q} \quad (13e)$$

$$\overline{w'\theta'_{z_i}} = -A_R \overline{w'\theta'_s} \quad (13f)$$

where $\bar{\theta}$ and $\bar{q}$ are the mean potential temperature and specific humidity in ML, $\overline{w'\theta'_s}$, $\overline{w'q'_s}$, $\overline{w'\theta'_{z_i}}$, and $\overline{w'q'_{z_i}}$ are the heat and moisture fluxes at the surface and the top of ML, respectively, w_e is the entrainment velocity, w_l is the mean upward large-scale velocity at the top

of the mixed layer, $\Delta\bar{\theta}$ and $\Delta\bar{q}$ are the potential temperature and specific humidity jump across the entrainment zone at the top of ML, and A_R is a flux ratio parameter constant set to be 0.2. The slab model uses a forward time-difference scheme.

The same surface heat flux $\overline{w'\theta'_s}$, moisture flux $\overline{w'q'_s}$ as for the transilient models are input as boundary conditions here. The initial potential temperature and specific humidity soundings in the free atmosphere (FA) as modified by subsidence are used to calculate $\Delta\bar{\theta}\,(=\theta_{z_i}|_{\text{sounding}} - \bar{\theta})$ and $\Delta\bar{q}\,(=q_{z_i}|_{\text{sounding}} - \bar{q})$ at each time step. The large-scale vertical motion at z_i is found from $w_l = (z_i/z_{\text{top}})w_s$, where z_{top} is the height of the top of the model where w_s is known.

5. Simulation results

a. Transilient–TKE model

Figure 5 shows simulated profiles of potential temperature θ and specific humidity q during the day of 28 May 1983. The ML evolution is clearly presented. A shallow stable layer forms after 1800 CDT, as indicated in Fig. 5a. Above 1000 m, the θ and q profiles change with height because of subsidence and advection.

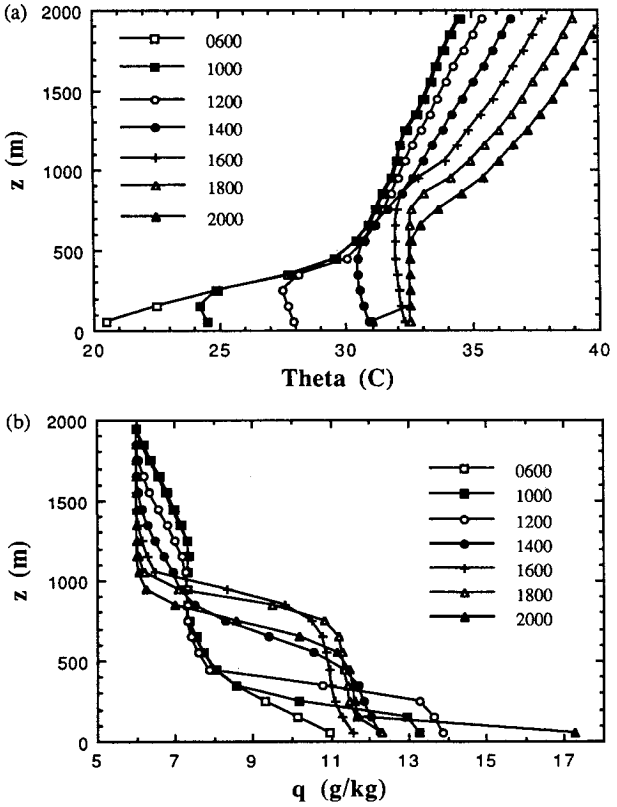

FIG. 5. Simulated evolution of vertical profiles of (a) mean potential temperature, theta; and (b) specific humidity, q, for 28 May 1983 from the transilient–TKE model. All times in the legends are local time in CDT.

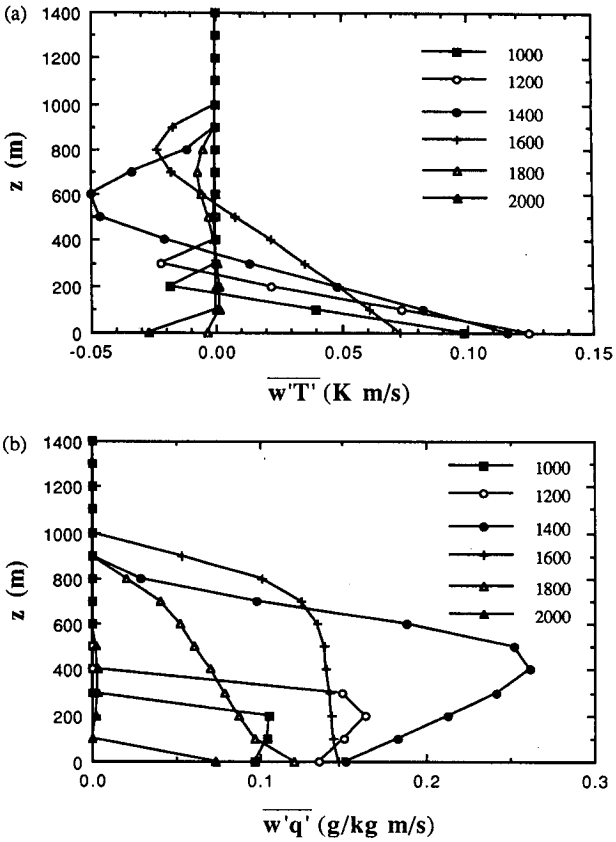

FIG. 6. Simulated evolution of vertical profiles of (a) heat flux $\overline{w'T'}$; and (b) moisture flux $\overline{w'q'}$ for 28 May 1983 from the transilient–TKE model. All times in the legends are CDT.

Heat flux $\overline{w'T'}$ and moisture flux $\overline{w'q'}$ profiles are shown in Fig. 6. Heat flux decreases approximately linearly with height within the ML during the free convection in the afternoon. The negative heat flux near the top of the ML is associated with the entrainment of warmer free-atmosphere air down into the ML. The near-vertical moisture flux profiles shown in Fig. 6b during afternoon is associated with evaporation from the ground and dry-air entrainment downward at the top of the ML. Turbulence starts to decay when the surface heat flux becomes negative at about 1800 CDT, as is evident in the change of heat flux profiles.

Figures 7 and 8 show simulated wind and momentum flux profiles during the day. Negative $\overline{u'w'}$ near surface in Fig. 8a is associated with a westerly wind speed increase with height in the lower ML (Fig. 7a). The large positive value of $\overline{u'w'}$ near the top of ML is related to the strong wind shear across the top of ML. The same phenomenon is observed for $\overline{v'w'}$ and V profiles near the top of ML.

b. Transilient–R_i model

Simulated profiles of potential temperature θ and heat flux $\overline{w'T'}$ are plotted in Fig. 9. The ML evolution

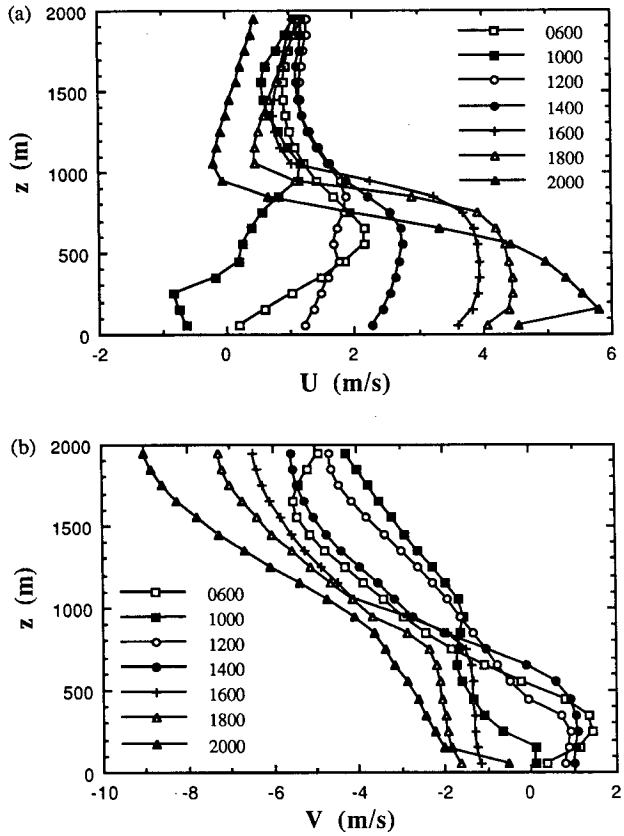

FIG. 7. Simulated evolution of vertical profiles of mean wind. (a) x component, U; and (b) y component, V, for 28 May 1983 from transilient-TKE model. All times in the legends are CDT.

is clearly presented in Fig. 9a. Compared with the TKE model (Fig. 5a), the R_i model gives a slightly shallower and more uniform ML, indicating a smaller turbulent domain with stronger mixing. This may be related to the neglect of turbulence dissipation in the definition of the R_i number. Comparing heat flux profiles of the TKE model (Fig. 6a) to the R_i model (Fig. 9b), the thick entrainment zone during the rapid rising phase at 1400 CDT in the TKE model appears later at 1600 CDT in the R_i model.

c. *Slab model*

Figure 10 shows the profiles of potential temperature θ and specific humidity q of the slab model. The heat flux profiles calculated from surface heat fluxes are shown in Fig. 11. They give a more gradual increase of ML.

d. *Comparison with observations*

The simulated profiles of potential temperature θ, specific humidity q, and wind U and V represent ensemble averages that should be equivalent to area averages over the horizontal domain of the field experiment. They are compared with rawinsonde soundings from Canton and Shawnee, Oklahoma, at 1400 and 1800 CDT, and with aircraft soundings at 1443 and 1735 CDT, shown in Figs. 12 to 15.

Modeled θ and q are nearly constant with height in the ML, as is typically observed, but are slightly shallower than the Shawnee and aircraft soundings and deeper than the Canton sounding. Modeled potential temperature agrees well with the Shawnee radiosonde sounding and the aircraft sounding, with an average difference of 1.5°C, while the Canton sounding deviates more because Canton is located farther away from the central field site. The average difference of specific humidity between the models and the observations is about 1.0 g kg^{-1} (excluding the Canton station).

Unlike the scalar variables, such as θ and q, which tend to be well mixed in ML, the vector variables U and V usually show a more complex structure and therefore more scatter between the observations and simulations. In Figs. 14 and 15, the averaged difference between observation and model is about 2–3 m s^{-1} for U and 1–2 m s^{-1} for V. The profiles of geostrophic wind are also shown in Fig. 14 and 15.

Time evolution of the observed surface potential temperature and specific humidity data from PAM II

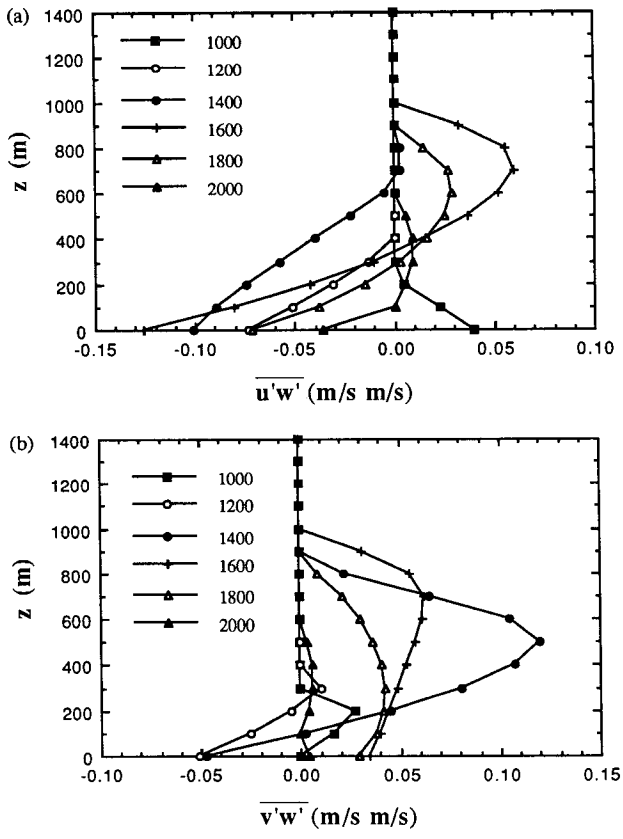

FIG. 8. Simulated evolution of vertical profiles of momentum fluxes. (a) in x direction $\overline{u'w'}$; and (b) in y direction, $\overline{v'w'}$ for 28 May 1983 from the transilient-TKE model. All times in the legends are CDT.

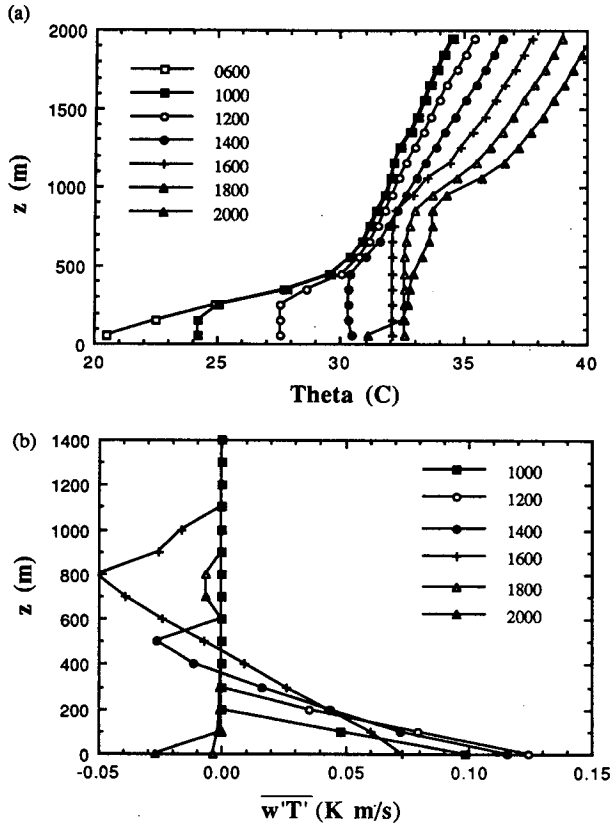

FIG. 9. Simulated vertical profiles of (a) potential temperature, theta, and (b) heat flux, $\overline{w'T'}$, from the transilient-R_i model for 28 May 1983. Times in legend are CDT.

are averaged over 13 stations, and compared with the lowest gridpoint results from the two transilient models (Fig. 16). The two parameterizations give surface forecasts in both θ and q that are close to each other but deviate slightly from the observations. Modeled surface temperature increases 12°C, due to surface heating and advection. A strong diurnal cycle of surface temperature is shown in Fig. 16a, with a maximum at 1700 CDT. In Fig. 16b, specific humidity increases 5 g kg^{-1}, due to surface evaporation during the day. The transilient models give a dry period around 1600 CDT, corresponding to strong entrainment of dry air from aloft, which is not observed in the data.

Figure 17 shows the verification of evolution of ML heights z_i during the day from three kinds of measurement and three models. The first observation uses lidar-measured averaged z_i from 1150 to 1716 CDT, where z_i is defined as the height where 50% of the air has free-atmosphere characteristics based on a horizontal average of scattered laser energy. The second observation is from θ and q radiosonde soundings at Canton, Shawnee, and Oklahoma City, assuming the top of the nearly constant θ and q layer is at z_i. The third one comes from aircraft soundings of θ and q at 1443, 1609, and 1735 CDT. The ML height z_i is determined from θ and q soundings by the height where the positive and negative areas balance above a slablike mixed layer (Driedonks 1982).

The forecasted values of z_i from the slab model are also plotted in Fig. 17. The transilient model z_i values are diagnosed from the simulated profiles, because the model is not a mixed-layer model and does not explicitly forecast z_i as in the slab model. Two kinds of z_i estimates from TKE model are plotted: the first is based on the height of the most negative heat flux ($\overline{w'T'}$), and the second from the shape of the θ and q profiles using Driedonk's method (1982). The estimate from the R_i model is based on the shape of θ and q profiles.

Lidar measurements indicate that z_i stays nearly constant around 580–720 m between 1200 and 1700 CDT, probably associated with strong subsidence, although the aircraft and rawinsonde soundings show continued depth increase. The transilient simulations show a rapid growth of z_i from 100 m during midmorning to 800 m later that afternoon, where the R_i parameterization shows a slightly shallow ML compared to the TKE parameterization. The slab model underestimates the ML height. Differences between these estimates are also partly due to the different definitions of z_i.

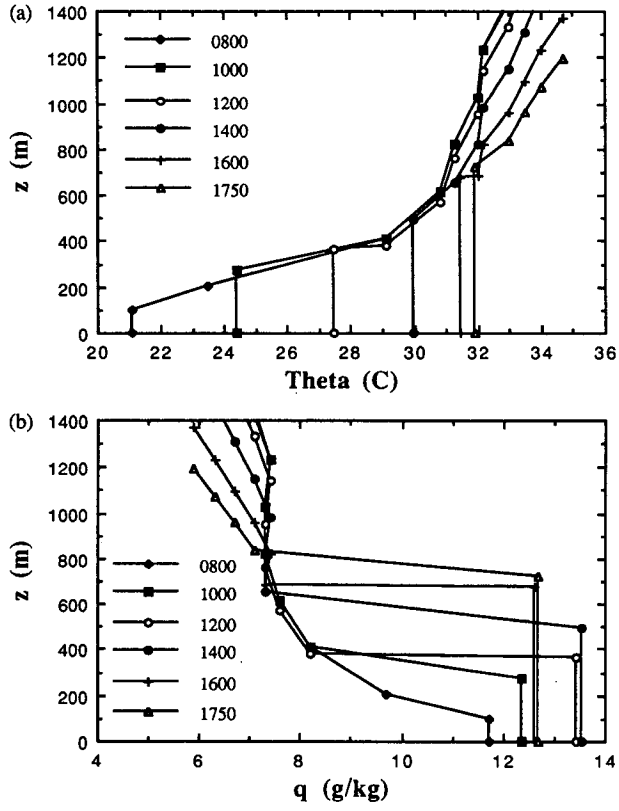

FIG. 10. Potential temperature and specific humidity profiles of 28 May 1983 from the slab model.

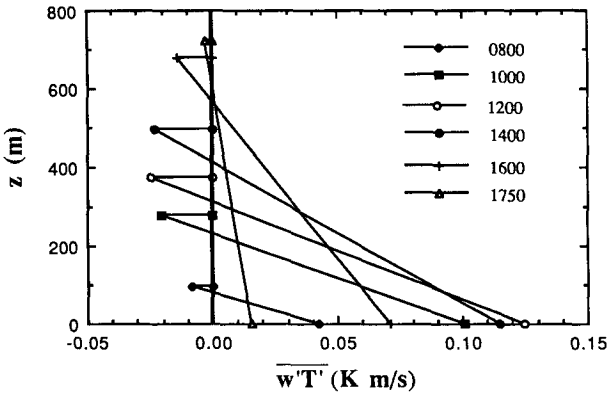

FIG. 11. Sensible heat flux profiles of 28 May 1983 from the slab model.

6. Spectral decomposition

a. Description

The mathematical description of transilient turbulence admits forms of nonlocal spectral composition that are not possible with traditional time series statistics of locally measured variables. Two kinds of spectra are calculated here: transport spectra $F(k, m)$ and process spectra PS (k, m) (Ebert et al. 1989).

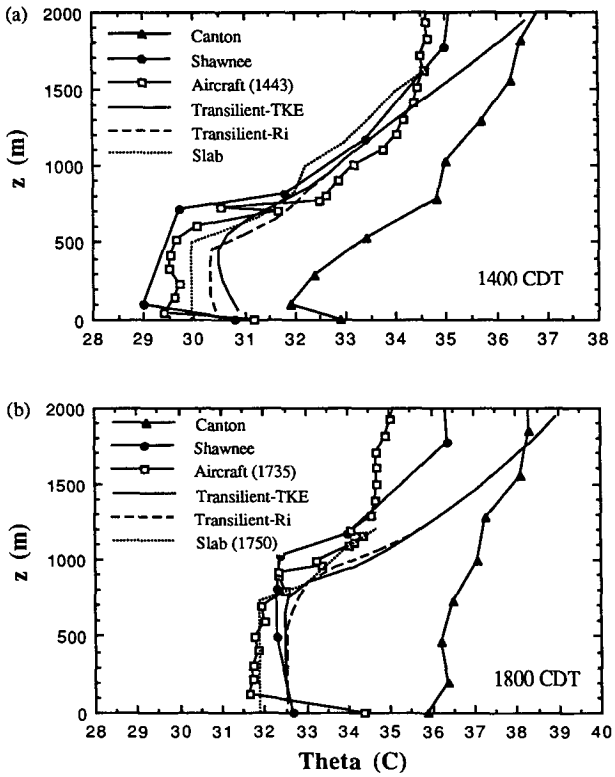

FIG. 12. Comparison of modeled potential temperature profile with observed radiosonde soundings and aircraft soundings on 28 May 1983: (a) at 1400 CDT and (b) at 1800 CDT.

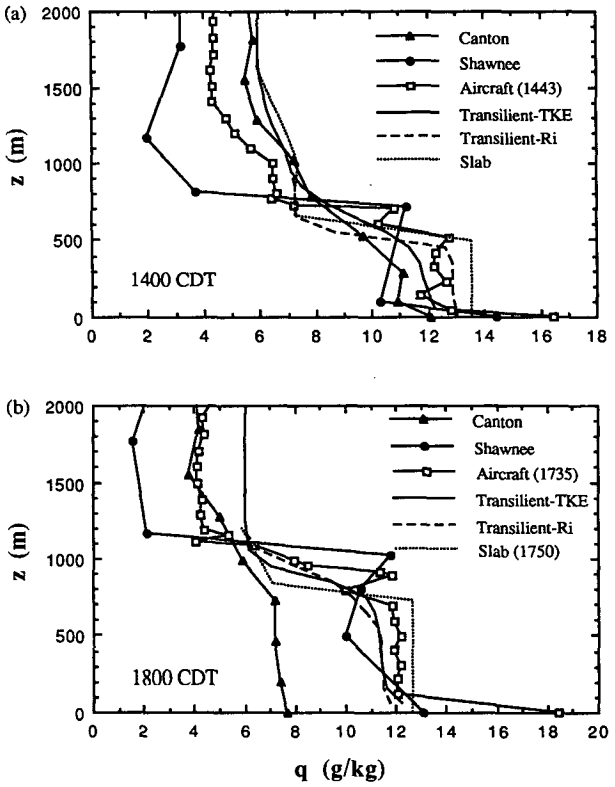

FIG. 13. Comparison of modeled specific humidity profile with observed radiosonde soundings and aircraft soundings on 28 May 1983: (a) at 1400 CDT and (b) at 1800 CDT.

The transport spectrum $F(k, m)$ indicates what portion of the total flux at height $z = k\Delta z$ is caused by mixing across that height between any source–destination grid locations separated by distance $\lambda = m\Delta z$, where k and m are integer indices. For the flux of tracer S during time step Δt, Ebert et al. showed that

$$F_s(k, m) = \frac{\Delta z}{\Delta t} \sum_{i=1}^{k} \sum_{j=k+1}^{N} \delta_{m,|i-j|}\, c_{ij}(t, \Delta t)[S_i - S_j] \tag{14}$$

where $\delta_{m,|i-j|}$ is the Kronecker delta and m is an integer between 1 and N. The total flux is the sum over all spectral components:

$$\overline{w's'}(k) = \sum_{m=1}^{N} F_s(k, m). \tag{15}$$

The process spectrum PS (k, m) sums the transilient coefficients associated with vertical mixing across height $k\Delta z$ between source–destination pairs separated by wavelength $m\Delta z$:

$$\mathrm{PS}(k, m) = \sum_{i=1}^{k} \sum_{j=k+1}^{N} \delta_{m,|i-j|}[c_{ij}(t, \Delta t) + c_{ji}(t, \Delta t)]. \tag{16}$$

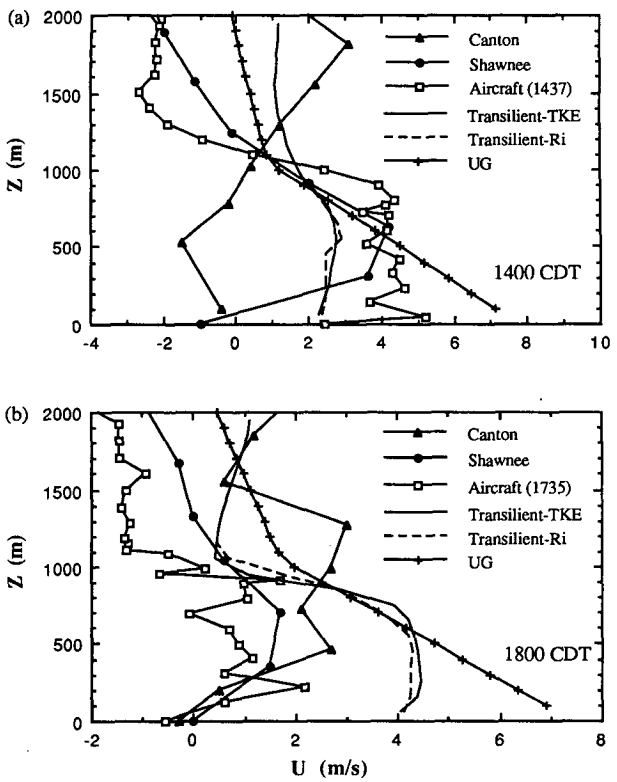

FIG. 14. Comparison of modeled wind U-component profile with observed radiosonde soundings and aircraft soundings on 28 May 1983: (a) at 1400 CDT and (b) at 1800 CDT.

In an environment of constant S with height, it is possible to have vigorous turbulence and mixing (large PS) with no flux of tracer S (zero F). The sum of PS over all spectral components, m, yields a mixing intensity, PS(k), that is the nonlocal analogy to the local vertical velocity variance:

$$\mathrm{PS}(k) = \sum_{i=1}^{k} \sum_{j=k+1}^{N} [c_{ij}(t, \Delta t) + c_{ji}(t, \Delta t)]. \quad (17)$$

Using output from the transilient forecast model (i.e., the coefficient matrix c_{ij} and variables θ, q, U, and V at each height) as input, setting $\Delta z = 100$ m, $\Delta t = 10$ min, and domain size = 2000 m, one can compute the spectral decomposition based on (14) through (17). We can find the contribution to heat flux $\overline{w'T'}$, moisture flux $\overline{w'q'}$, and momentum flux $\overline{u'w'}$ and $\overline{v'w'}$ from different size eddies ranging from 100 m to 1000 m, at different levels from the surface to the top of ML.

b. *Results from transilient-TKE*

1) TRANSPORT SPECTRA

Figure 18 shows the profiles of nondimensional heat flux at 1600 CDT. The heat fluxes are normalized by the surface heat flux that is imposed as a boundary condition (see Fig. 2). The normalized total heat flux (thick line) decreases linearly from the surface to the most negative value at $1.0z_i$, then to zero around $1.4z_i$. It agrees with the universal profiles based on similarity theory (Stull 1988). The contributions of different wavelengths to the total flux at different heights are clearly presented. Each curve has two peaks of different sign. Small eddies ranging from 100 to 200 m (i.e., 0.13 to $0.25z_i$) contribute mostly to positive flux in the surface layer, which is related to strong turbulent mixing near surface (see process spectra Fig. 21), and to negative flux at the top of the ML, which is associated with the large lapse rate in the entrainment zone. These small eddies contribute virtually nothing to the fluxes near the middle of the mixed layer. Similarly, 300–400-m (i.e., 0.38–$0.5z_i$) eddies contribute the most to the fluxes corresponding to heights of 300 m (i.e., $0.37z_i$) (positive) and 700 m (i.e., $0.88z_i$) (negative). Since the ML height z_i is 800 m at 1600 CDT, the 900–1000-m eddies do not exist.

Figure 19 gives the nondimensional moisture flux profiles at 1400 CDT. The peak of total moisture flux at 420 m ($0.7z_i$) is associated with the large decrease of q with height in ML; that is, moist air is mixing upward and dry air is mixing downward (see Fig. 5b),

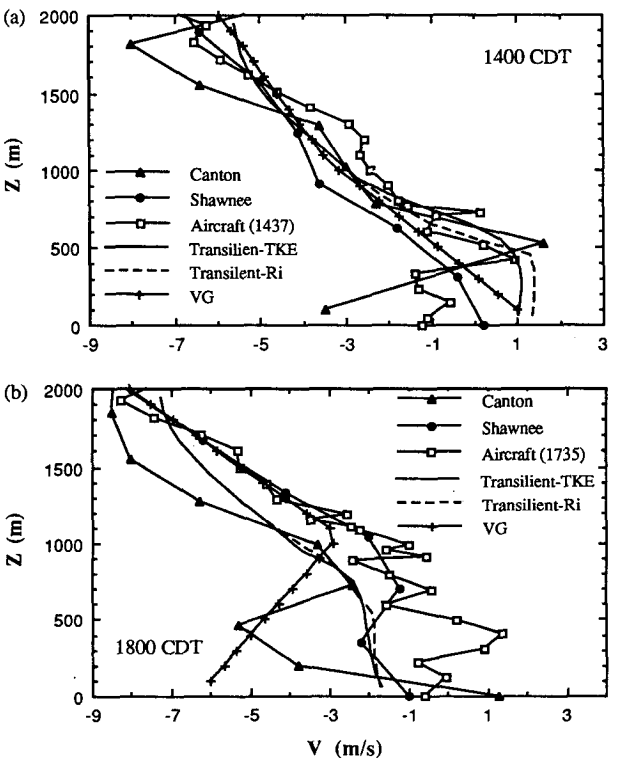

FIG. 15. Comparison of modeled wind component V profile with observed radiosonde soundings and aircraft soundings on 28 May 1983: (a) at 1400 CDT and (b) at 1800 CDT.

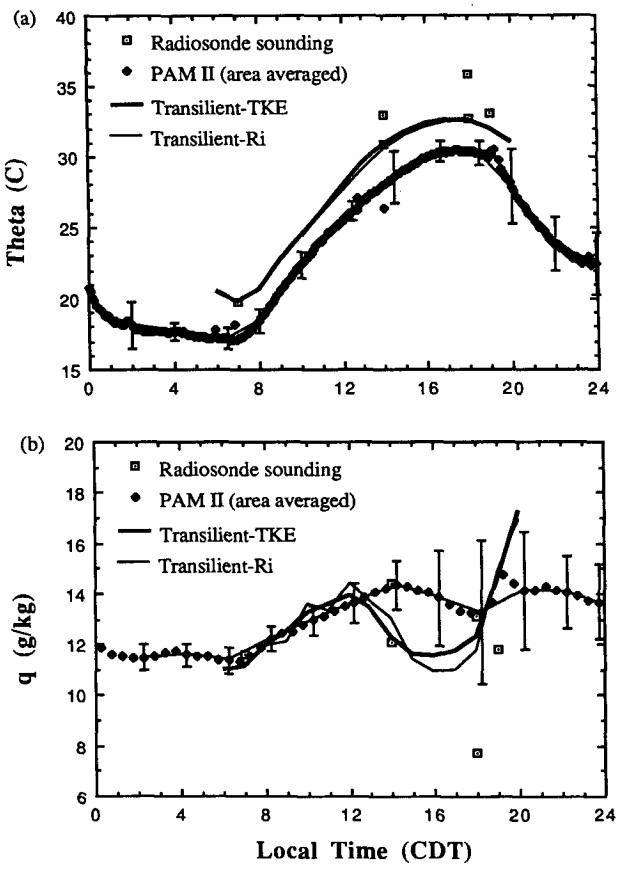

FIG. 16. Comparison of time series of modeled and observed (PAM II and radiosonde soundings) surface mean (a) potential temperature and (b) specific humidity for 28 May 1983. Bars indicate the standard deviation of the PAM II measurements.

and is also associated with the "rapid-rise" phase of ML at 1400 CDT. There are two peaks in the flux profiles, at wavelength 100–200 m (0.13–$0.25z_i$) and 300–400 m (0.38–$0.5z_i$), due to strong mixing near the surface and the large q gradient at the top of ML. For wavelengths larger than 500 m, the profiles exhibit one peak where wavelength $m\Delta z$ equals height z, and the peaks become broader as the wavelength increases. Again, the larger eddies dominate near the middle of the mixed layer.

A better understanding of the role of eddies of different sizes can be gained by examining their variation with time. For example, at 100 m, 400 m, and 800 m, the contribution of different wavelengths to heat flux are plotted as a function of time (Fig. 20). For a height of 100 m (Fig. 20a), heat fluxes of all wavelengths are positive, which reflects the surface sensible heat flux input as a boundary condition. The peak of total flux at 100 m has a two-hour time lag compared with surface boundary conditions $(\overline{w'T'})_s$ in Fig. 2. The peaks shift along the time axis as wavelengths increase. This also indicates that thermals are rising to greater heights.

For a height of 400 m (Fig. 20b), the total heat flux is negative prior to 1430 CDT, because the ML height is 680 m at 1430 CDT, and the top portion of ML is always associated with negative heat flux. After 1430 CDT, heat fluxes become positive for all wavelengths, showing that the ML is growing upward away from 400 m.

At a height of 800 m, near the top of ML (Fig. 20c), the heat flux is negative due to warm air aloft mixing down to the top of ML for all sizes of eddies. At 1800 CDT, after surface sensible heat flux supply stops, heat fluxes go to zero at 100 m and 400 m, and remain a small negative value at 800 m.

2) PROCESS SPECTRA

Figure 21 shows the process spectra at 1400 CDT. Similar to transport spectra, the smallest eddies are the most important at lower heights. As height increases, the peaks become broader, less intense, and shift to the larger wavelengths that are related to large thermals (long wavelengths) rising from the warm surface to the top of ML. The medium and smaller scales are associated with the cascade of turbulence energy, giving the broader peaks near z_i (Ebert et al. 1989).

Spectra analysis provides a clearer picture of the contributions of different size eddies to the total flux at different times. A nonlocal spectral decomposition of the fluxes at different levels indicates that the eddies with size $\lambda = m\Delta z$ contribute the most to the total flux at height $z = m\Delta z$. It is a helpful tool for understanding the ML structure and ML evolution.

7. Summary and conclusions

Transilient turbulence theory (Stull 1984) is a nonlocal closure scheme for turbulence parameterization. This paper tests two versions of a one-dimensional transilient simulation model against data collected in the BLX83 field experiment in Oklahoma during the summer of 1983. A slab mixed-layer model is also tested.

A cloudless day, 28 May 1983, with sufficient measurements from instrumented aircraft, radiosonde, PAM II stations, and flux tower was chosen for this case study. These measurements supply the initial conditions and boundary conditions of the model, and they allow verification of the simulated results. Because no tuning of parameters was performed for this study, it represents another independent verification of the TKE closure parameterization for transilient turbulence theory.

Simulated potential temperature θ, specific humidity q, and winds are well mixed in the interior of the ML, and θ increases with height in the entrainment zone. The modeled potential temperature θ differs by an average of 1.5°C from the radiosonde and aircraft sound-

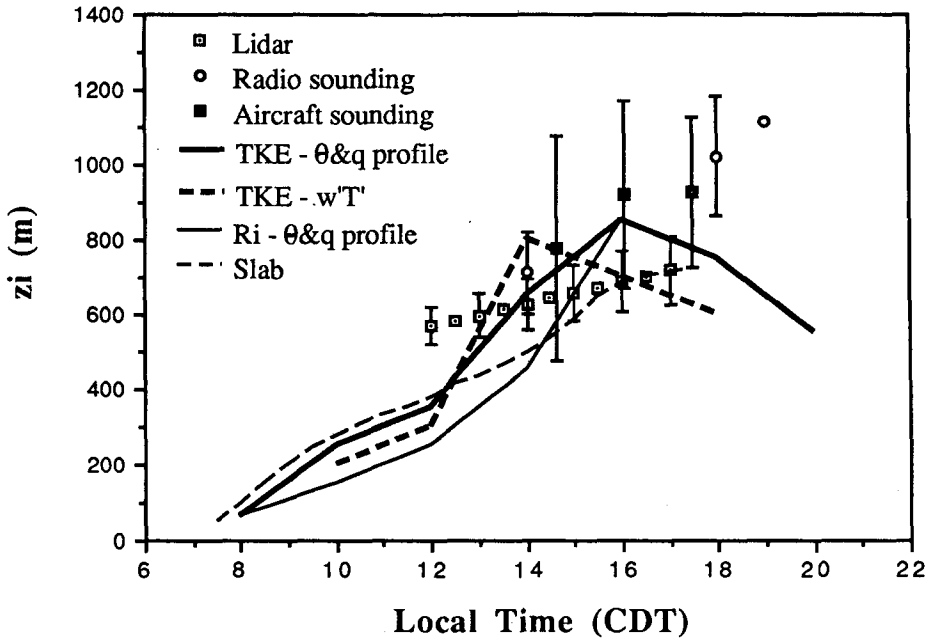

FIG. 17. Comparison of three modeled and three observed boundary-layer heights z_i vs time on 28 May 1983. Bars represent sampling errors.

ings, the specific humidity q has an average of 1.0 g kg^{-1} difference from the observations, and there is a 1–3 m s^{-1} difference between simulated and observed wind components at 1400 CDT and 1800 CDT (excluding Canton). Modeled heat flux decreases approximately linearly with height. The large amount of negative heat flux at the top of ML at 1400 CDT (Fig. 6a) occurs during the rapid height increase of the ML. The flux during this highly nonstationary period is not captured by classical slab mixed-layer models, but is well described by the transilient model. Modeled moisture flux profiles show a large value near the top of ML at 1400 CDT as expected. The shape of momentum flux profiles is associated with the corresponding wind profiles.

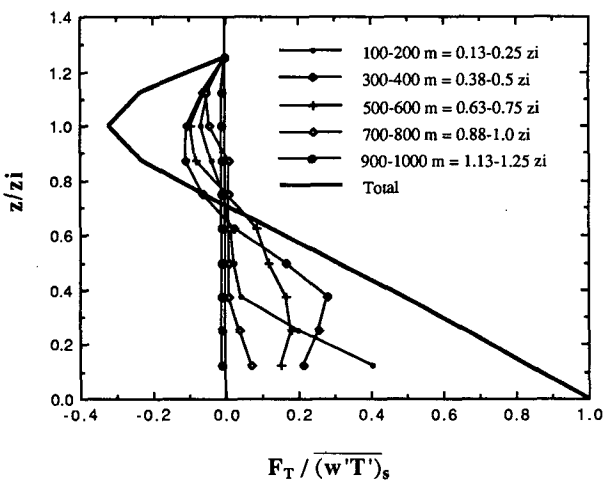

FIG. 18. Contributions of different-size eddies to the total heat fluxes at different heights at 1600 CDT 28 May 1983. Heat fluxes are normalized by the observed surface heat flux (Fig. 2). Heights are normalized by z_i (800 m) from the transilient simulation model (Fig. 17).

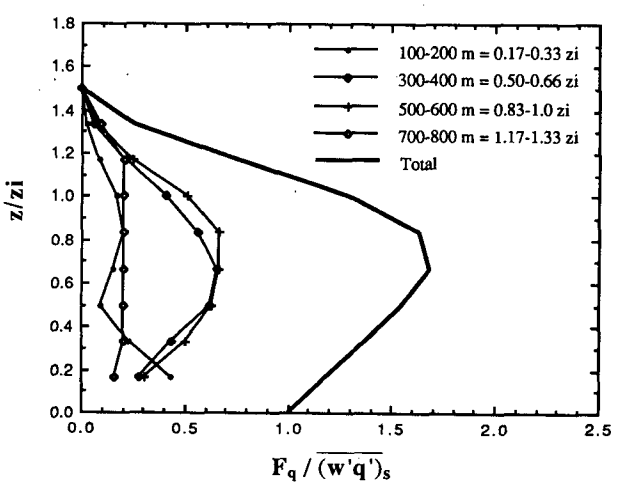

FIG. 19. Contributions of different-size eddies to the total moisture fluxes at different heights at 1400 CDT 28 May 1983. Moisture fluxes are normalized by the observed surface moisture flux (Fig. 2). Heights are normalized by z_i (600 m) from the transilient simulation model (Fig. 17).

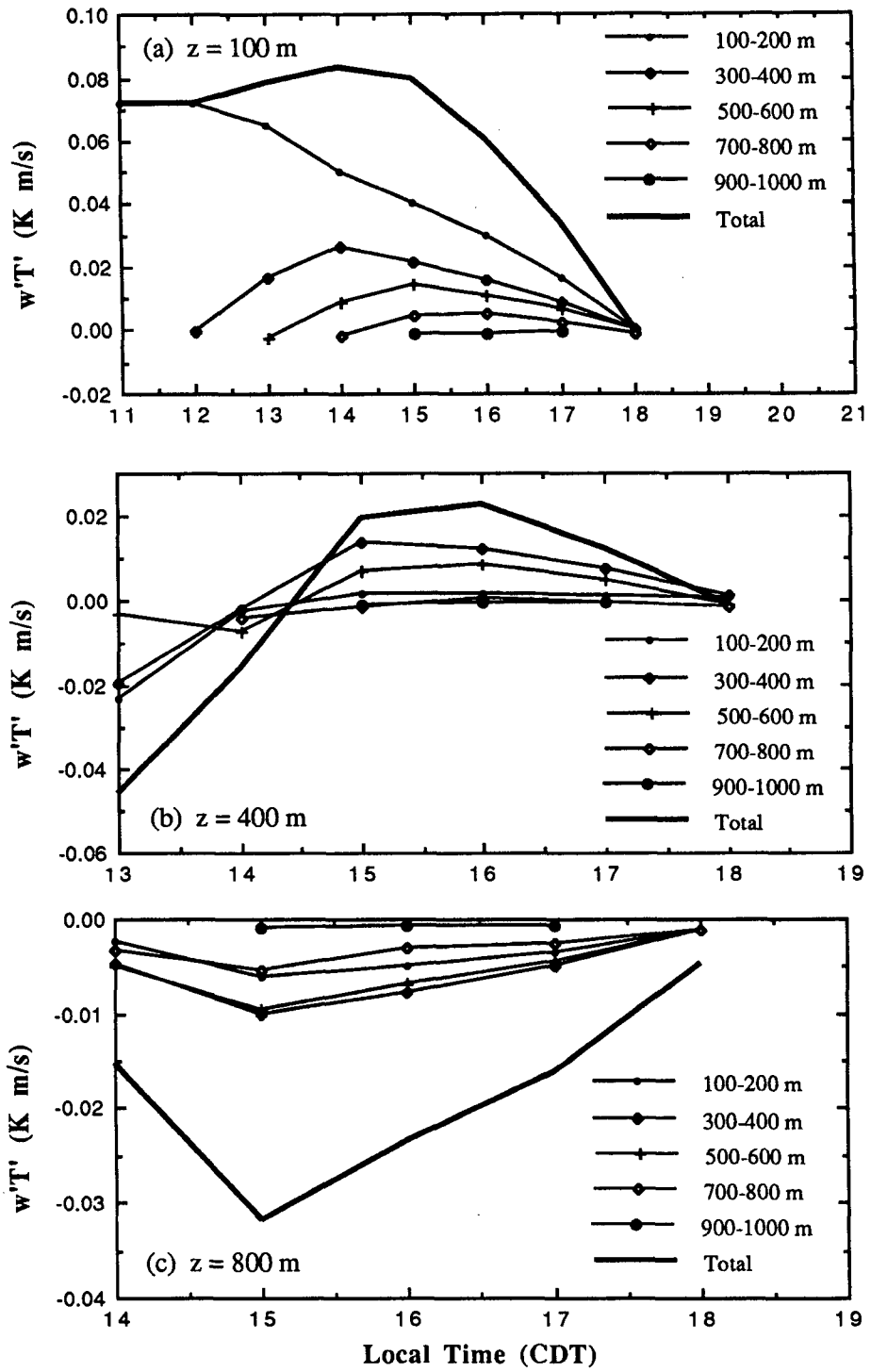

FIG. 20. Contributions of different-size eddies to the total heat flux across levels at (a) 100 m, (b) 400 m, and (c) 800 m vs time (CDT) on 28 May 1983.

There is no explicit forecast equation for ML depth z_i in the transilient model; hence, z_i must be diagnosed from simulated profiles. The model exhibits a shallow ML at 1000 CDT that becomes much deeper by 1600 CDT. Transilient model-simulated ML height z_i is between that of the radiosonde and aircraft soundings

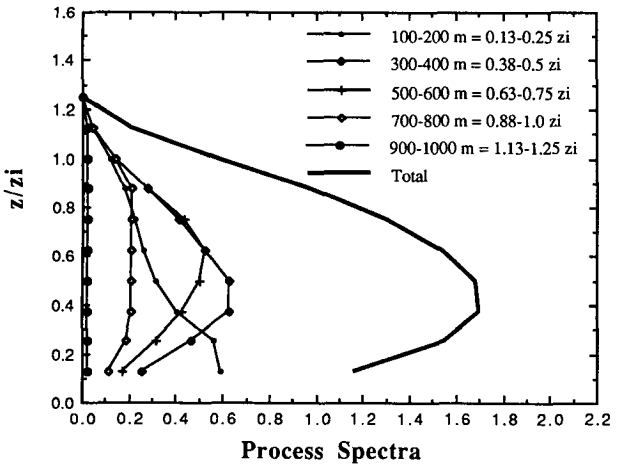

FIG. 21. Decomposition of different-size eddies to the total process spectrum vs height at 1400 CDT 28 May 1983.

and the lidar measurements. Modeled surface potential temperature θ and specific humidity q evolution are close to the PAM II and radiosonde observations.

Spectral decomposition provides a useful tool to understand the mechanism of turbulence exchange. It shows that the contributions of different-size eddies to the total fluxes depend on the height within the ML and the time of day. Eddies contribute the most to the total flux at the corresponding height of their size. At any fixed altitude, the peaks of the total flux shift along the time axis as wavelengths increase, indicating that the ML is rising. The medium- and large-size eddies contribute significantly to the total flux, particularly near the middle of the mixed layer where smaller-size eddies contribute virtually nothing.

From the comparison with BLX83 field experiment data, the transilient simulation model shows a good agreement to the observations in potential temperature θ, specific humidity q, and wind profiles U and V, as well as ML height z_i evolution.

Both parameterizations of the transilient coefficient matrix c_{ij} reduce a matrix of n^2 coefficients to a function of several parameters, and both assume c_{ij} is symmetric. The TKE version is a bit more complicated but includes more physical process than the relatively simple R_i version. The R_i version gives more realistic temperature profile within the surface layer and mixed layer for convective conditions than does the TKE version. These parameterizations still cannot capture some characteristics of turbulence structure explained by the matrix asymmetry reported by Ebert et al. (1989).

Acknowledgments. The BLX83 experiment was conducted by UW-Madison, Argonne National Lab, NCAR, and National Severe Storms Lab. This research was supported by National Science Foundation (NSF) Grant ATM-8822214. NCAR is sponsored by NSF.

APPENDIX

Estimate of Surface Heat and Moisture Fluxes from Observations of ANL Flux Tower and Queen Air Aircraft

Figure 22 shows the observed half-hour–averaged surface sensible and latent heat fluxes, net radiation from the ANL flux tower (square points), and the near-surface sensible and latent heat fluxes from the Queen Air aircraft five surface legs (solid dots). A second-order polynomial fit yields the best fit for the flux tower data in this case. Due to the systematic errors of underestimating of the magnitudes from the flux tower data, this whole set of data are used to provide the diurnal tendency of the fluxes. The aircraft data determine the magnitude of the fluxes. The final fluxes are obtained by fixing the two zero points of the flux tower curves and amplifying the curves to match the aircraft flux measurements.

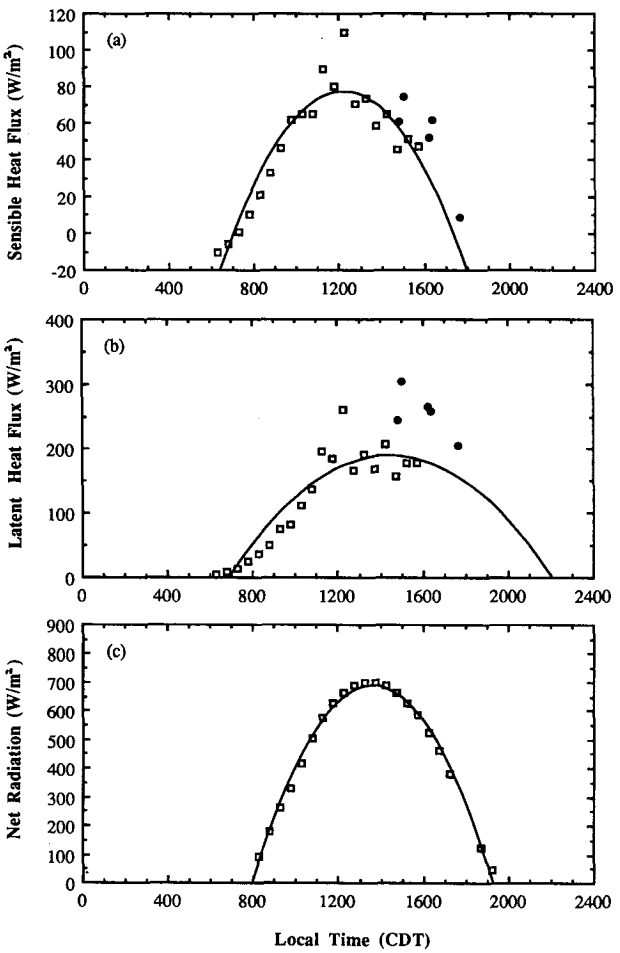

FIG. 22. Observed half-hour averaged surface (a) sensible heat flux, (b) latent heat flux, and (c) net radiation R_n from ANL flux tower on 28 May 1983. The three curves are from second-order polynomial fits.

REFERENCES

Crum, T. D., 1985: Case studies of the structure of the atmospheric boundary layer entrainment zone, Ph.D. thesis, Dept. of Atmos. and Oceanic Sci., University of Wisconsin—Madison, Madison, WI.

——, and R. B. Stull, 1987: Field measurements of the amount of surface layer air versus height in the entrainment zone. *J. Atmos. Sci.*, **44,** 2743–2753.

——, ——, and E. W. Eloranta, 1987: Coincident lidar and aircraft observations of entrainment into thermals and mixed layers. *J. Climate Appl. Meteor.*, **26,** 774–788.

Driedonks, A. G. M., 1982: Models and observations of the growth of the atmospheric boundary layer. *Bound.-Layer Meteor.*, **23,** 283–306.

Ebert, E. E., U. Schumann, and R. B. Stull, 1989: Nonlocal turbulent mixing in the convective boundary layer evaluated from large-eddy simulation. *J. Atmos. Sci.*, **46,** 2178–2207.

Ferrare, R. A., 1984: Lidar observations of organized convection within the atmospheric mixed layer. M.S. thesis, Dept. of Atmos. and Oceanic Sci., University of Wisconsin—Madison, Madison, WI.

Hechtel, L. M., 1988: Large-eddy simulations of the effects of nonhomogeneous surface fluxes on the planetary boundary layer. M.S. thesis, Dept. of Atmos. and Oceanic Sci., University of Wisconsin—Madison, Madison, WI.

——, C. H. Moeng, and R. B. Stull, 1990: The effects of nonhomogeneous surface fluxes on the convective boundary layer: A case study using large-eddy simulation. *J. Atmos. Sci.*, **47,** 1721–1741.

Louis, J. F., 1979: A parametric model of vertical eddy fluxes in the atmospheric. *Bound.-Layer Meteor.*, **17,** 187–202.

Nelson, E., R. B. Stull, and E. W. Eloranta, 1989: A prognostic relationship for entrainment zone thickness. *J. Climate Appl. Meteor.*, **28,** 885–903.

Stull, R. B., 1984: Transilient turbulence theory. Part I: The concept of eddy-mixing across finite distance. *J. Atmos. Sci.*, **41,** 3351–3367.

——, 1987: Transilient turbulence algorithms to model mixing across finite distances. *Environmental Software,* **2,** 4–12.

——, 1988: *An Introduction to Boundary Layer Meteorology.* Kluwer Academic, 666 pp.

——, and E. W. Eloranta, 1984: Boundary-Layer Experiment—1983, *Bull. Amer. Meteor. Soc.*, **65,** 450–456.

——, and T. Hasegawa, 1984: Transilient turbulence theory, Part II: Turbulent adjustment. *J. Atmos. Sci.*, **41,** 3368–3379.

——, and A. G. M. Driedonks, 1987: Applications of the transilient turbulence parameterization to atmospheric boundary layer simulations. *Bound.-Layer Meteor.*, **40,** 209–239.

Vachalek, R. E., 1987: Case studies of divergence and vertical velocities calculated using different sensing systems, M.S. thesis, Dept. of Atmos. and Oceanic Sci., University of Wisconsin—Madison, Madison, WI.

Wilde, N. P., R. B. Stull, and E. W. Eloranta, 1985: The LCL zone and cumulus onset. *J. Climate Appl. Meteor.*, **24,** 640–657.

Zhang, Q., 1990: Test of transilient turbulence theory against a field experiment. M.S. thesis, Dept. of Atmos. and Oceanic Sci., University of Wisconsin—Madison, Madison, WI.